


## Article

# Study on Atmospheric Water Resource Variation Characteristics in China and Influencing Factors of Precipitation Efficiency of Hydrometeors

Lin An, Zhanyu Yao , Pei Zhang, Shuo Jia, Jieyun Zhao, Zhen Liu and Zequn Zhang

CMA Cloud-Precipitation Physics and Weather Modification Key Laboratory, China Meteorological Administration Weather Modification Center, Beijing 100081, China

\* Correspondence: yaozy@cma.gov.cn

**Abstract:** Understanding the spatial and temporal variation characteristics of atmospheric water resources in each region of China is essential for their exploitation. In this study, we focus on the variation in atmospheric precipitable water (PW), cloud parameters, cloud water resources (CWR), and precipitation efficiency of hydrometeors (PEh) as well as their possible influencing factors in each region of China in summer using ERA5 and MODIS data. The results showed that: (1) In the past 42 years, PW increased significantly in the northwest and Tibetan Plateau regions, and both cloud cover and total column cloud water content decreased significantly in northern China, except for medium-cloud cover which significantly increased in the Tibetan Plateau. (2) In the past 20 years, annual PEh was significantly higher, with clear interdecadal variation in most regions, whereas CWR decreased in northern China, the southwest, central region, and southeast, and increased in northeast and Tibetan Plateau. (3) PEh in each region was greatly influenced by precipitation (correlation coefficient  $0.55 < R < 0.82$  \*, \* =  $p < 0.05$ ), having a significant positive correlation in the northeast with cloud water path, cloud optical thickness, and aerosol optical depth ( $0.44 < R < 0.54$  \*), and a significant negative correlation in the central region with the cloud effective radius ( $R = -0.54$  \*).

**Keywords:** atmospheric water resource; cloud water resources; precipitation efficiency of hydrometeors; variation characteristics; influencing factors



**Citation:** An, L.; Yao, Z.; Zhang, P.; Jia, S.; Zhao, J.; Liu, Z.; Zhang, Z. Study on Atmospheric Water Resource Variation Characteristics in China and Influencing Factors of Precipitation Efficiency of Hydrometeors. *Water* **2023**, *15*, 1020. <https://doi.org/10.3390/w15061020>

Academic Editor: Paul Kucera

Received: 31 January 2023

Revised: 23 February 2023

Accepted: 27 February 2023

Published: 8 March 2023



**Copyright:** © 2023 by the authors. Licensee MDPI, Basel, Switzerland. This article is an open access article distributed under the terms and conditions of the Creative Commons Attribution (CC BY) license (<https://creativecommons.org/licenses/by/4.0/>).

## 1. Introduction

Since the 1990s, due to global climate change and economic and social development inducing a series of chain reactions such as an increase in population and ecological degradation, solving the problem of water shortages has become one of the prerequisites for social and economic development in China today, requiring immediate attention. Precipitation from clouds is an important sustainable atmospheric water resource (AWR). Therefore, understanding the status of AWR and variation trends in different regions of China is of great strategic importance for the scientific and rational exploitation of AWR, resulting in the alleviation of water shortages, improving the ecological environment, and ensuring sustainable economic and social development [1].

AWR consists of atmospheric water vapor and cloud water resources (CWR) [2]. Water vapor is the material basis of precipitation. It not only affects the precipitation weather and climate of each region, but also influences water circulation and the energy balance of the land and atmosphere through advection and vertical transport as well as evaporation and condensation [3].

As an important source of atmospheric water resources, there are many studies on water vapor [4,5]. Some scholars have studied the spatial and temporal characteristics of atmospheric water vapor content in the arid zone of northwest China (NW) [6–8]. Others have studied the evolutionary characteristics of water vapor content in the Tibetan Plateau

(TP) [9–11]. Water vapor cannot form precipitation directly; it is converted into cloud water that becomes precipitation through condensation or deposition.

Cloud water is a potential water resource residing in the atmosphere in the form of clouds, that can be exploited and utilized by humans. As clouds are the main targets of weather modification, understanding regional variations in cloud cover and cloud water content (CWC) plays a key role in the exploitation of local CWR. Several findings on cloud parameters and CWR have been obtained [12–17], and some studies based on ground station observations showed an overall decrease trend in total cloud cover (TCC) and low-cloud cover (LCC) in the past decades [18–20]. Owing to China's complex topography and limited ground stations, especially in the western and highland regions [21,22], accurate observations of clouds over the whole of China are difficult. Satellite remote sensing is the most direct and effective way to obtain spatial and spectral information at local and global scales, and it has been widely used to study cloud parametric changes [23–27]. In particular, studies using the International Satellite Cloud Climatology Project (ISCCP) and Moderate-resolution Imaging Spectro-radiometer (MODIS) data show that TCC and medium-cloud cover (MCC) increased in eastern China and decreased in western China, and LCC and high-cloud cover (HCC) decreased in most regions over the past few decades [28,29]. Annual mean low-cloud CWC generally decreased, whereas CWC was highest in June, lowest in October, and increased overall [1].

Some scholars also found that cloud cover in east-central China during the daytime in summer significantly decreased from 2001 to 2017 based on cloud observations from the Clouds and the Earth's Radiant Energy System (CERES) [30]. In recent years, some scholars have studied the variability characteristics of AWR in different regions of China using reanalysis information provided by the European Centre for Medium-range Weather Forecasting (ECMWF) [31–33]. For example, You et al. [34] showed that CWC increased in non-monsoonal regions and TP in the summer from 1979 to 2016. Cheng et al. [35] showed that over five major watersheds located in the "Asian water tower" between 2000 and 2017, CWR was lower and decreasing in the Indus River Basin, while it was higher and increasing in the Yangtze River Basin and Yellow River Basin.

Precipitation efficiency [36] is an important indicator for characterizing AWR conversion and an important parameter for measuring the potential for AWR exploitation. Based on previous studies, it is mainly divided into the precipitation efficiency of water vapor and the precipitation efficiency of hydrometeors (PEh) [37–39]. Zhang et al. [40] found that, in the arid NW region between 1979 and 2013, the precipitation efficiency of water vapor was basically stable until 2002 and increased significantly from 2003 to 2013. A recent study showed that there were significant seasonal differences in PEh and CWR in different regions of China [41].

To date, many scholars have studied the variation characteristics of AWR in different regions of China, but due to the lack of early accurate observations of cloud water, most of them only focus on water vapor resources, while relatively few studies look at CWR, especially PEh. In addition, most existing studies have focused on a small area, and there is a lack of research on multi-temporal variation in CWR for all China's regions. Following the normal Chinese administrative divisions, we divided China into seven regions (as shown in Figure 1) to study the regional variability of AWR characteristics. Our specific method of division was based on An et al. [2]. First, we studied the long-term trends of atmospheric precipitable water (PW), cloud cover, and total column CWC in China, based on which we further analyzed the multi-timescale variation of characteristic quantities of CWR in each region. Finally, we preliminarily explored the possible factors affecting PEh in each region. The above work can serve as a reference for the scientific and rational exploitation of AWR in China, which can help to alleviate water shortages, improve the ecological environment, and ensure sustainable socio-economic development.

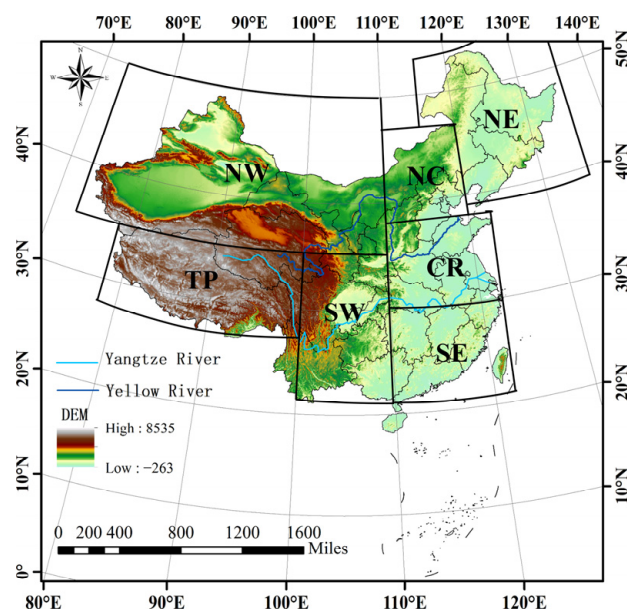


**Figure 1.** Topographic map of China. The polygons indicate the seven sub-regions defined as Northwest China (NW), North China (NC), Northeast China (NE), Tibetan Plateau (TP), Southwest China (SW), Central Region (CR), and Southeast China (SE). The inner filled colors are the Digital Elevation Model (DEM), the data of which are from Resource and Environment Science and Data Center, and the spatial resolution is 250 m.

## 2. Data and Methods

### 2.1. Data

In this study, a combination of ground precipitation, reanalysis, and satellite data was considered. Surface precipitation data were obtained from the  $0.5^\circ \times 0.5^\circ$  daily surface precipitation dataset V2.0 (June–August 2001–2020) provided by the National Meteorological Information Center of China [42]. This dataset was based on precipitation data from China’s ground-based high-density stations (2472 national meteorological observation stations) compiled by the National Meteorological Information Center’s Basic Data Project, which was spatially interpolated in real time, has good conditions for error analysis, and has been well used in several studies [34,43].

The reanalysis data we used were the ERA5 monthly averages data [44] from 1979 to 2020 and every six hours (four times a day at 0000, 0600, 1200, and 1800 UTC) data [45] in summer (June to August) from 2001 to 2020 released by the ECMWF. ERA5 has a higher horizontal resolution (30 km) than its predecessor ERA-Interim (79 km), is divided vertically into 137 levels, and has an upper pressure of 1 hPa that better reflects the observed global climate changes [46]. It was widely used in recent years [47–49]. Climate-related elements included PW, total column cloud liquid-water content (TCLWC), total column cloud ice-water content (TCIWC), TCC, HCC, MCC, and LCC, as well as the wind field and specific CWC field (including specific cloud liquid-water content and specific cloud ice-water content) in each layer. The spatial resolution was  $0.25^\circ \times 0.25^\circ$ .

We also used the Terra satellite Level-3 MODIS Atmosphere Daily Global Product MOD08\_D3 (June–August) from 2001 to 2020 [50] which has a spatial resolution of  $1^\circ \times 1^\circ$ . This dataset has high confidence and accuracy due to rigorous processing and quality control at the NASA Goddard data archive center, and it is widely used in cloud parameter studies [51–53]. The required cloud parameters were cloud water path (CWP), cloud optical thickness (COT), cloud effective radius ( $R_e$ ), cloud top temperature (CTT), cloud top pressure (CTP), and land and ocean aerosol optical depth (AOD) at 550 nm.

## 2.2. Methodology

### 2.2.1. Calculation of Characteristic Quantities Related to CWR

The CWR characteristic quantities defined in this paper included precipitation (P), total atmospheric hydrometeors (Gh), CWR, and PEh, and the meanings and calculation methods of them are described in the same way as in An et al. [2].

### 2.2.2. Least Squares Fit and Correlation Analysis

To study the trends of each climate-related element, we used the least squares method [54], to solve the linear equation in two unknowns  $x = bt + a$  to fit the data series  $x(t), t = 1, 2, \dots, n$ , wherein  $t$  represents the time series,  $n$  represents the number of years,  $a$  is a constant, and  $b$  is a regression coefficient. If  $b$  is a positive value, it indicates an increasing trend of the element with the time series, and if it is negative, it indicates a decreasing trend, and the larger  $|b|$  is, the more pronounced the trend is. The Pearson correlation coefficient ( $R$ ) [54] is often used as an indicator to test the significance of the linear trend. We found that when the number of years  $n = 42$  (1979–2020),  $|R| > 0.3$  indicates that the trend passed the significance test at the 95% confidence level, and when  $n = 20$  (2001–2020),  $|R| > 0.44$  indicates that the trend passed the significance test at the 95% confidence level.

In addition, the  $R$  was used to study the degree of linear correlation between two meteorological elements. In this study, for two elements  $x$  and  $y$  with a sample size of  $n$ , by estimating the covariance and standard deviation of the sample, the  $R$  can be obtained. If  $R$  is positive, it indicates that the two variables are positively correlated, and if  $R$  is negative it indicates that they are negatively correlated, and the higher  $|R|$  is, the stronger the correlation.  $|R| > 0.8$  is defined as a high correlation,  $0.5 \leq |R| \leq 0.8$  shows medium correlation,  $0.3 \leq |R| < 0.5$  shows low correlation, and  $|R| < 0.3$  is a slight correlation. The significance of the correlation coefficient was tested using the  $t$  statistic. Given a significance level  $\alpha = 0.05$ , the correlation coefficient is considered to pass the significance test if  $t$  meets  $|t| \geq t_\alpha$ .

### 2.2.3. Mann–Kendall Trend Test

The Mann–Kendall (M–K) trend test [55,56] is a rank-based nonparametric test for the presence of a monotonic trend in a time series. In the M–K trend test, for a time series with a sample size of  $n$ , the order column of the M–K test is calculated as follows:

$$S = \sum_{j=1}^{n-1} \sum_{i=j+1}^n \text{sgn}(x_i - x_j) \quad (1)$$

where  $x_i$  and  $x_j$  denote the values at the moments when the time series is  $i$  and  $j$ ;  $0 < j < i < n$ ; and  $\text{sgn}(x_i - x_j)$  is calculated as follows:

$$\text{sgn}(x_i - x_j) = \begin{cases} 1, & x_i - x_j > 0 \\ 0, & x_i - x_j = 0 \\ -1, & x_i - x_j < 0 \end{cases} \quad (2)$$

The variance of  $S$ ,  $\text{var}(S)$ , is calculated as follows:

$$\text{var}(S) = \frac{1}{18} \left[ n(n-1)(2n+5) - \sum_{p=1}^g t_p(t_p-1)(2t_p+5) \right] \quad (3)$$

where  $g$  is the number of tied groups, and  $t_p$  is the number of identical values in a tied group. If the sample size is  $n > 10$ , then the statistic for the M–K test  $Z_c$  is calculated as follows:

$$Z_c = \begin{cases} \frac{S-1}{\sqrt{\text{var}(S)}}, & S > 0 \\ 0, & S = 0 \\ \frac{S+1}{\sqrt{\text{var}(S)}}, & S < 0 \end{cases} \quad (4)$$

If  $Z_c$  is positive, it means that the time series has an increasing trend, and if it is negative, then it has a decreasing trend. For the trend test in this study, given a significance level  $\alpha$ ,  $|Z_c| \geq Z_{1-\alpha/2} = 1.96$  indicates that the trend passes the significance test at the 95% confidence level.

We also used Sen’s slope [57] to calculate the extent of the time series trend. Sen’s slope  $\beta$  is calculated as follows:

$$\beta = \text{Median} \left( \frac{x_i - x_j}{i - j} \right), \forall j < i \quad (5)$$

where  $\beta > 0$  indicates a positive trend change;  $\beta < 0$  indicates a negative trend change; and the magnitude of  $\beta$  indicates the rate of change.

### 3. Results and Analysis

#### 3.1. Long-Term Trends of PW across the Four Seasons

Wang et al. [58] comprehensively evaluated the global reliability and accuracy of PW provided by five atmospheric reanalysis products and showed that the ERA5 product had the highest accuracy and best performance. Therefore, this study uses ERA5 data to reliably analyze the changing characteristics of PW in China. Figure 2 shows the distribution of monthly average PW for all seasons in China from 1979 to 2020. For each season, the high value area of PW is SE, and the low value areas are TP, the Tianshan and Qilian Mountains, and other high-altitude areas. PW was more abundant in summer. In terms of the long-term trend (Figure 3), in summer, the rate of change of PW was faster and increased in most of the regions compared with other seasons. There was a notable increase in PW in the NW and TP and no notable increase in NC, NE, SW, and CR.

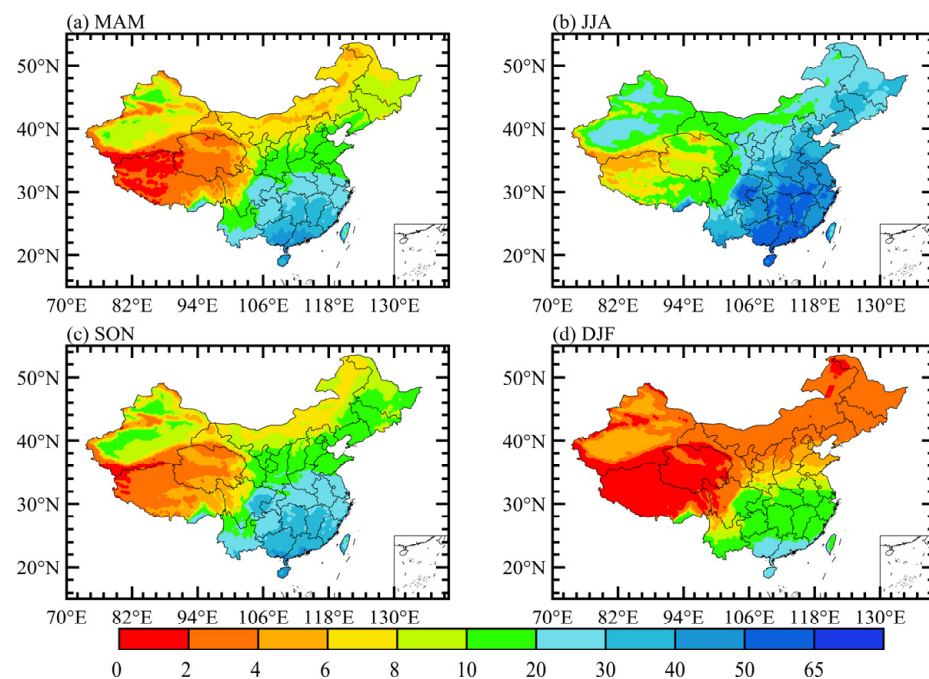


**Figure 2.** Spatial distribution of seasonal average atmospheric precipitable water (PW) over China during 1979–2020 (unit: kg·m<sup>-2</sup>). (a) Spring, (b) Summer, (c) Autumn, (d) Winter.

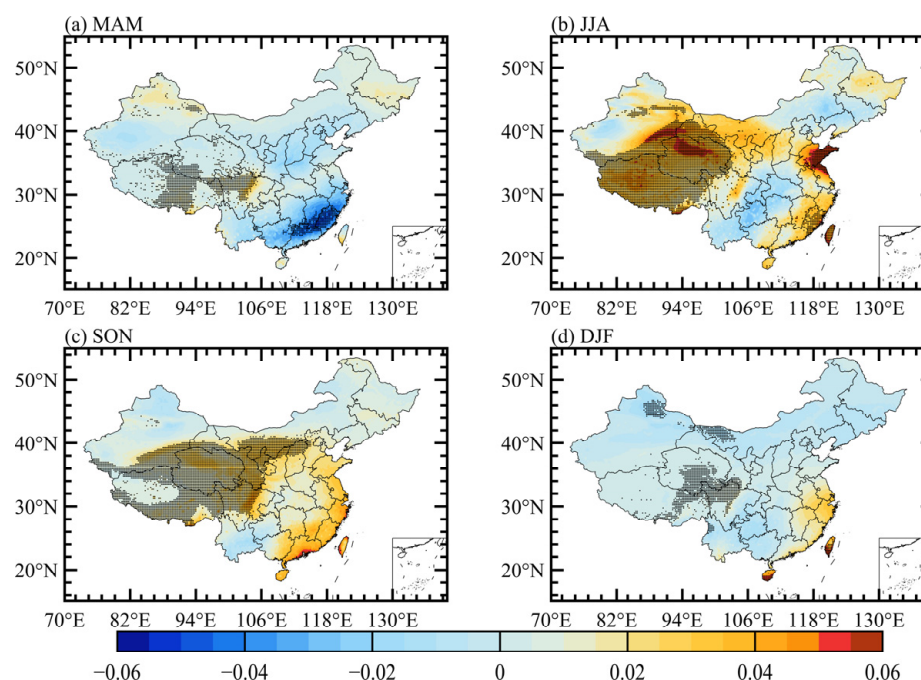


**Figure 3.** Spatial distribution of seasonal PW trends over China during 1979–2020 (unit:  $\text{kg}\cdot\text{m}^{-2}\cdot\text{yr}^{-1}$ ). The stippled areas indicate that the trends passed the significance test at the 95% confidence level. (a) Spring, (b) Summer, (c) Autumn, (d) Winter.

The above analysis of the distribution and long-term trend of the climatic state of PW in China in all seasons reveals that water vapor content is more abundant in all regions in summer compared with other seasons, and the regions where water vapor content changes at a faster rate and passes the significance test are also significantly larger. Evidently, it is of great practical importance to study the variation in AWR in summer; therefore, the following research on cloud parameters and CWR characteristic quantities focused on the summer period only.

### 3.2. Long-Term Trends of Cloud Cover and CWC in Summer

Zhang et al. [59] conducted a comparative analysis using multiple reanalysis data and ISCCP data with actual observations in China and found that the total cloud cover measurements of ERA5 had the highest agreement with ground observations, with a correlation coefficient of 0.91. Therefore, in this study, we used ERA5 data to study the cloud cover characteristics of China's regions. Figure 4 shows the distribution of monthly mean cloud cover in summer from 1979 to 2020. It can be seen that the mountain ranges such as the Tianshan, Qilian, and the Kunlun Mountains had good cloud-cover conditions. TCC and LCC had similar distributions, with more cloud cover in TP, SW, and SE, and less in the NW and NC (Figure 4a,d); HCC decreased from south to north, with the high value area located in SW and the low value area on the Kunlun Mountains and in surrounding areas (Figure 4b); MCC was greater in the TP and SW, and lower in the NW (Figure 4c).

Similarly, analysis of the trends in cloud cover (Figure 5) revealed that TCC, HCC, and LCC were broadly similar, with a long-term notable increase in TP and decrease in the other regions. Specifically, TCC and HCC decreased markedly in NC, NE, and CR, as did TCC in SW, and LCC in NC, CR, SW, and SE (Figure 5a,b,d). The rate of change of MCC was slower than the other three types of cloud cover, and it increased notably in the Qaidam Basin and decreased notably in NC (Figure 5c).

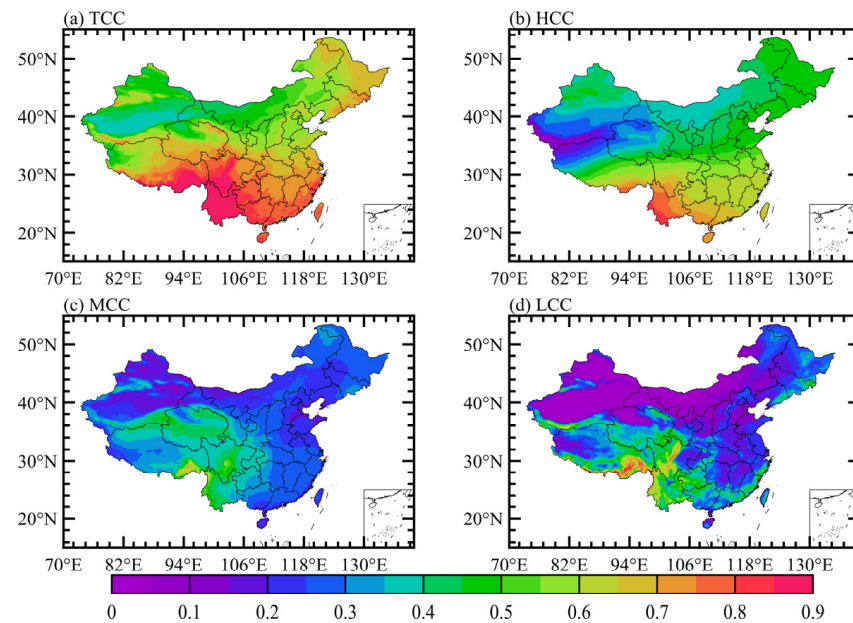


**Figure 4.** Spatial distribution of monthly average (a) total cloud cover (TCC), (b) high-cloud cover (HCC), (c) medium-cloud cover (MCC) and (d) low-cloud cover (LCC) over China during the summers of 1979–2020.

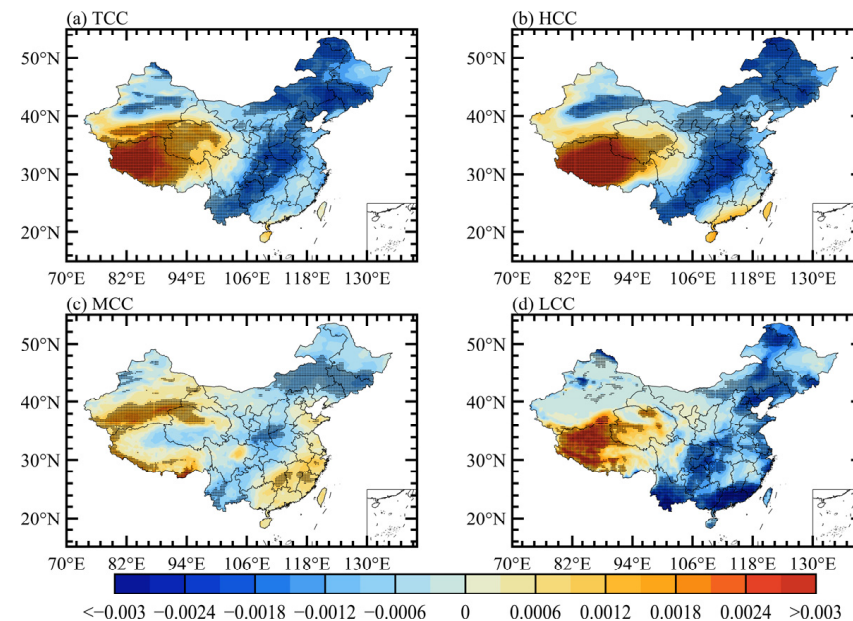


**Figure 5.** Spatial distribution of (a) TCC, (b) HCC, (c) MCC, and (d) LCC trends over China during the summers of 1979–2020 (unit:  $\text{yr}^{-1}$ ). The stippled areas indicate that the trends passed the significance test at the 95% confidence level.

Taylor et al. [60] and Shupe et al. [61] showed that CWC has an important effect on the radiative properties of clouds and characterizes the abundance of AWR. Figure 6 shows the distribution of monthly average total column CWC in summer. CWC tended to be higher along mountain ranges. TCLWC decreased from the south and SW to the NW, and the high value area was the SW; another high value center was in southeast TP. TCLWC was lower in the TP and NW (Figure 6a). The distribution of TCIWC has a high degree of similarity to TCC, namely, it was higher in the SW and lower in the NW, with the Yangtze River Delta being a high value area (Figure 6b).

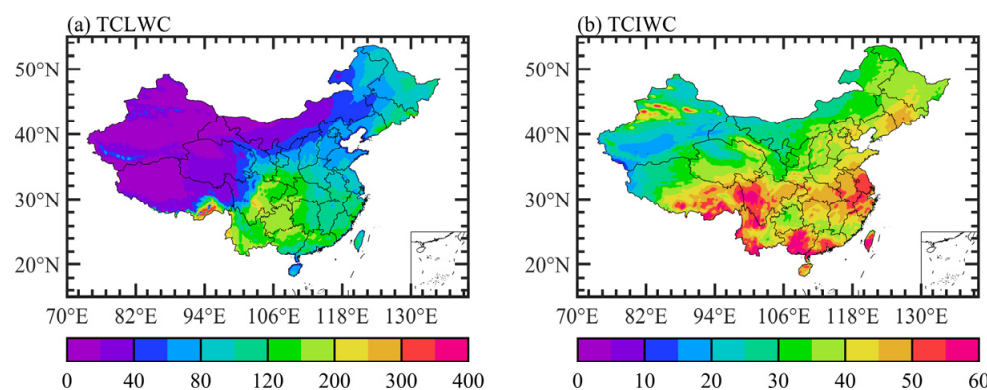


**Figure 6.** Spatial distribution of monthly average total column of (a) cloud liquid-water content (TCLWC) and (b) cloud ice-water content (TCIWC) over China during the summers of 1979–2020 (unit:  $\text{g}\cdot\text{m}^{-2}$ ).

The long-term trend of total column CWC shows that both TCLWC and TCIWC decreased significantly in NC. In addition, there was a significant increase in TCLWC in TP, and the rate of change was faster in the southeast area of TP. Areas with long-term decreases in TCLWC were roughly similar to those where cloud cover decreased, i.e., mainly coastal areas in SW and SE and the Changbai Mountains area (Figure 7a). There was a long-term significant increase in TCIWC in TP and a long-term significant decrease in NE, SW, and CR (Figure 7b).

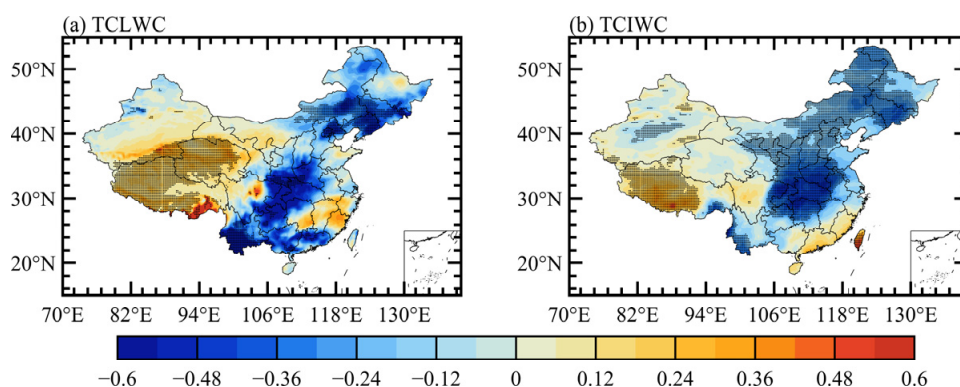


**Figure 7.** Spatial distribution of (a) TCLWC and (b) TCIWC trends over China during the summers of 1979–2020 (unit:  $\text{g}\cdot\text{m}^{-2}\cdot\text{yr}^{-1}$ ). The stippled areas indicate that the trends passed the significance test at the 95% confidence level.

### 3.3. Multi-Timescale Changes of CWR Characteristic Quantities in Each Sub-Region in Summer

The above analysis of the changes in PW, cloud cover, and total column CWC in China during the summers over a period of 42 years revealed that trends and rates of change differed significantly among regions. We further analyzed the multi-timescale variation characteristics of CWR characteristic quantities in each sub-region of China in summer. Owing to limited data, we selected 2001–2020 as the study period. Figure 8 shows the distributions of summer multi-year averages of P, Gh, CWR, and PEh. Gh and CWR were more abundant in the NE, CR, and SE and lower in the NW and TP (Figure 8b,c). The high-value area of PEh was the main part of TP. PEh was also relatively high in the SW and SE, and the low-value area was still the NW (Figure 8d). Thereafter, we analyzed the variation in characteristic quantities of CWR in each sub-region in summer at three scales: annual, monthly, and 10 days.



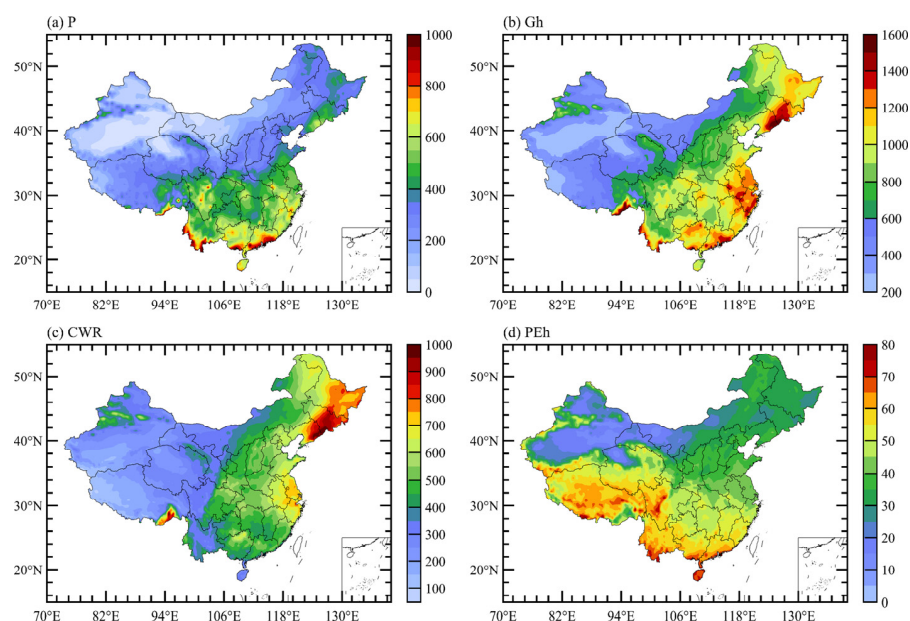


**Figure 8.** Spatial distribution of summer annual average of (a) total surface precipitation (P, unit: mm), (b) total atmospheric hydrometeors (Gh, unit: mm), (c) cloud water resource (CWR, unit: mm) and (d) precipitation efficiency of hydrometeors (PEh, unit: %) in China during the summers of 2001–2020.

### 3.3.1. Annual Variations

Figure 9 shows the distribution of linear changing trends of CWR characteristic quantities in summer in China over the last 20 years. P, Gh, and CWR had roughly similar patterns of variation, with annual decreases in the Changbai Mountain region, and the southeastern coastal region, and significant increases in the Yangtze River Delta (Figure 9a–c). PEh variation was roughly bounded by  $97.5^{\circ}$  E, with an increasing trend east of that line and a decreasing trend west of it. PEh also significantly decreased in the Tarim Basin and significantly increased in the Sichuan Basin (Figure 9d).

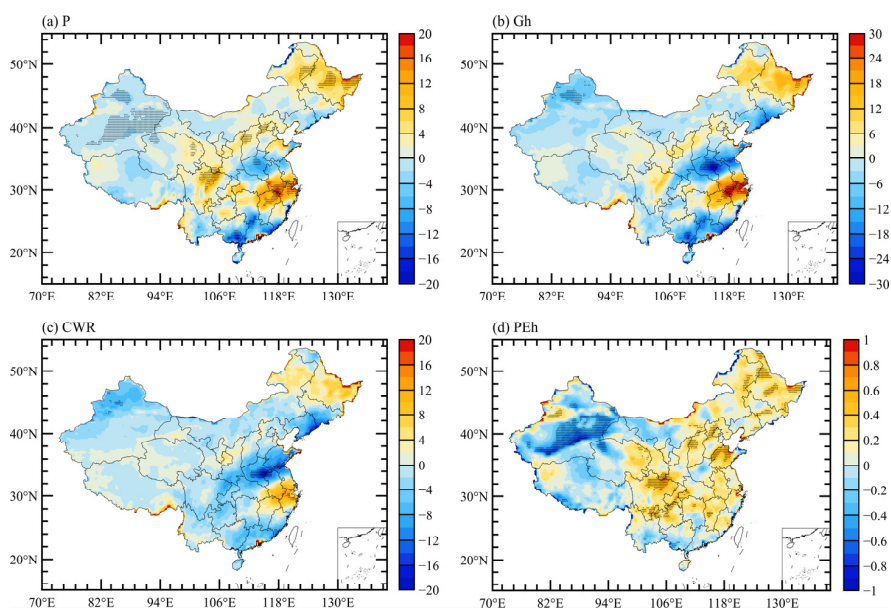


**Figure 9.** Spatial distribution of summer annual linear changing trends of (a) P (unit:  $\text{mm}\cdot\text{yr}^{-1}$ ), (b) Gh (unit:  $\text{mm}\cdot\text{yr}^{-1}$ ), (c) CWR (unit:  $\text{mm}\cdot\text{yr}^{-1}$ ) and (d) PEh (unit:  $\%\cdot\text{yr}^{-1}$ ) in China during the summers of 2001–2020. The stippled areas indicate that the trends passed the significance test at the 95% confidence level.

Table 1 quantifies the magnitude of the summer annual variations of CWR characteristic quantities in each region. The trend in a certain region was considered significant in this study when its confidence levels of both the least squares regression and the M–K test were greater than or equal to 95%. The trend was considered as being of little variation if the least squares trends were positive and M–K test trends were negative. P showed increasing trends in all regions except CR where there was little variation. Gh displayed increasing trends in the NE, TP, SW, and SE, a decreasing trend in CR, and little variation in the NW and NC. The increasing trends of CWR existed in the NE and TP, while decreasing trends were in NC, SW, CR, and SE, and little variation in the NW. For PEh, there were increasing trends in all regions except TP with a small decrease, and the NW with little variation.

**Table 1.** Summer annual changing trends of P, Gh, CWR, and PEh in the seven sub-regions of China during the summers of 2001–2020. The  $b$  and  $\beta$  represent the least squares regression and M–K test trends, and the \* indicates that the trends passed the significance test at the 95% confidence level.

Region	P (mm·yr <sup>-1</sup> )		Gh (mm·yr <sup>-1</sup> )		CWR (mm·yr <sup>-1</sup> )		PEh (%·yr <sup>-1</sup> )	
	$b$	$\beta$	$b$	$\beta$	$b$	$\beta$	$b$	$\beta$
NW	0.25	0.16	−1.17	1.1	−1.43	0.83	0.08	−0.02
NC	1.29	1.13	−0.24	0.06	−1.53	−2.56	0.19	0.22
NE	4.07 *	3.67 *	6.46	5.75	2.39	1.1	0.22	0.26
TP	0.68	0.27	1.87	1.35	1.19	1.68	−0.08	−0.07
SW	3.17	2.64	0.78	1.35	−2.39	−1.29	0.26 *	0.25
CR	1.04	−0.92	−2.96	−5.53	−4	−4.77	0.2	0.22
SE	2.52	3.54	0.04	1.72	−2.48	−1.92	0.24 *	0.29 *

The overall trends may offset the short-term variation. Figure 10 shows the time series variations of CWR characteristic quantity anomalies in the sub-regions in different years. In NW, Gh and CWR were significantly higher in 2001 and mostly lower thereafter (Figure 10(b<sub>1</sub>,c<sub>1</sub>)). In NC, the P, Gh, and CWR did not vary significantly until 2012, and then they were significantly higher in 2012 and 2013 and significantly lower in 2014 and 2015 (Figure 10(a<sub>2</sub>,b<sub>2</sub>,c<sub>2</sub>)). In the NE, the Gh and CWR were predominantly lower until 2011, and then significantly increased in 2012 and 2013, then decreased from 2014 to 2017, and increased again in the following three years (Figure 10(b<sub>3</sub>,c<sub>3</sub>)). In the TP, the Gh and CWR were predominantly low until 2013, however, after 2013 they showed predominantly positive anomalies (Figure 10(b<sub>4</sub>,c<sub>4</sub>)). In SW, the Gh and CWR were significantly high in 2001 and predominantly low thereafter (Figure 10(b<sub>5</sub>,c<sub>5</sub>)). In CR, the P, Gh, and CWR were predominantly high until 2008, with a significant increase in 2003, then were mostly low after 2008, until another significant increase in 2020 (Figure 10(a<sub>6</sub>,b<sub>6</sub>,c<sub>6</sub>)). In SE, the P, Gh, and CWR were significantly high in 2001 and 2002, with mostly negative anomalies thereafter (Figure 10(a<sub>7</sub>,b<sub>7</sub>,c<sub>7</sub>)).

PEh had clear interdecadal variations in all regions, with very low PEh in 2001, and four different statuses of PEh distribution thereafter: in the NW, after 2002, PEh was mostly high across all years (Figure 10(d<sub>1</sub>)); in the NC, NE, and SE, in the first 10 years, the PEh was predominantly low, while it increased with more positive anomalies in the next 10 years (Figure 10(d<sub>2</sub>,d<sub>3</sub>,d<sub>7</sub>)); in the TP, in the first 10 years, the PEh was mostly high, and there was not a large difference between positive and negative anomalies in the second 10 years (Figure 10(d<sub>4</sub>)); and finally in the SW and CR, negative anomalies of PEh were more frequent and larger in the years before 2004, and mostly positive anomalies thereafter (Figure 10(d<sub>5</sub>,d<sub>6</sub>)).

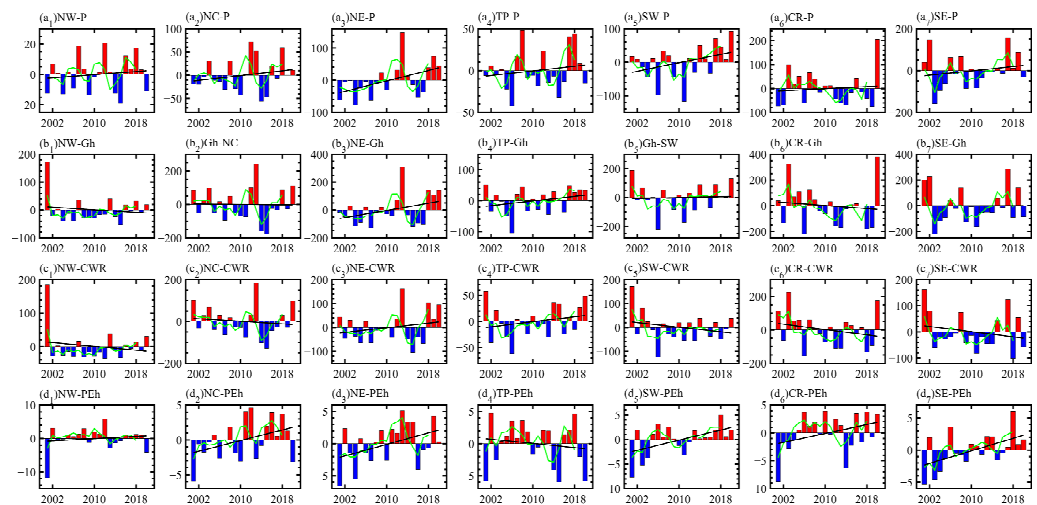


**Figure 10.** Summer annual time series variations of anomalies of (a<sub>1</sub>–a<sub>7</sub>) P (unit: mm·yr<sup>-1</sup>), (b<sub>1</sub>–b<sub>7</sub>) Gh (unit: mm·yr<sup>-1</sup>), (c<sub>1</sub>–c<sub>7</sub>) CWR (unit: mm·yr<sup>-1</sup>), and (d<sub>1</sub>–d<sub>7</sub>) PEh (unit: %·yr<sup>-1</sup>) in the seven sub-regions of China during the summers of 2001–2020. The green curve is a 3-year moving average, and the black line is the least squares linear trend.

### 3.3.2. Monthly Variations

On shortening the time scale of the study to monthly variations in summer, it was revealed that P and Gh were higher in July in most regions, while Gh was higher in June in the southern regions, and P was also higher in the SE in June (Figure 11a,b). CWR was higher in July and August in the NC and NE, and in June in the southern regions and CR, while it did not vary much in the NW and showed a decreasing monthly trend in TP (Figure 11c). The summer variations of PEh in the three northern regions were mainly between 20% and 40% with a smaller monthly change, less than those in the southern regions, CR, and TP, which were mainly between 40% and 70%, and consistently higher in July and August (Figure 11d).

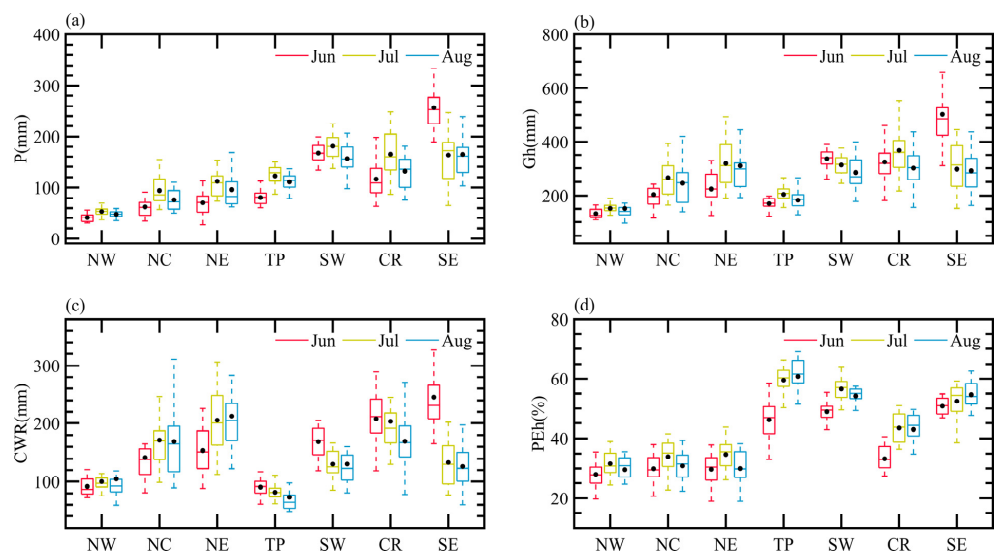


**Figure 11.** Box plot of summer monthly variations of (a) P, (b) Gh, (c) CWR, and (d) PEh in the seven sub-regions of China during the summers of 2001–2020. Solid lines in the boxes represent the median (Q3); the upper and lower sides of the boxes represent the upper quartile (Q4) and lower quartile (Q2), respectively; the upper and lower ends of the boxes' lines represent 1.5 times greater than the interquartile range (IQR = Q4–Q2) of the Q4 and 1.5 times less than the IQR of the Q2, representing outliers; and the black dots in the boxes represent the mean values.

### 3.3.3. Ten-Day Variations

The study scale was further shortened to the ten-day scale in summer, and we can see that all characteristic quantities showed a ten-day increasing trend in June and did not vary much in July and August in the NW. In both the NC and NE, the P, Gh and CWR were highest in late July. In TP, the P had a ten-day increasing trend in June and July, and almost no change in August; Gh showed an increasing trend in June, and almost no change in July and August; and CWR demonstrated a ten-day decreasing trend in July. In the southern regions, both Gh and CWR decreased from early June to late July, and Gh and CWR increased in the SW and did not vary much in the SE in August. In the CR, Gh increased in both June and August and decreased in July, and CWR was higher in late June (Figure 12a–c).

PEh first increased and then decreased in summer in all regions except the SE. In the TP, SW, and CR, the range of PEh variation was large, with high values in late July and early August. The range of PEh variation in the SE was small, with an overall increasing trend (Figure 12d).

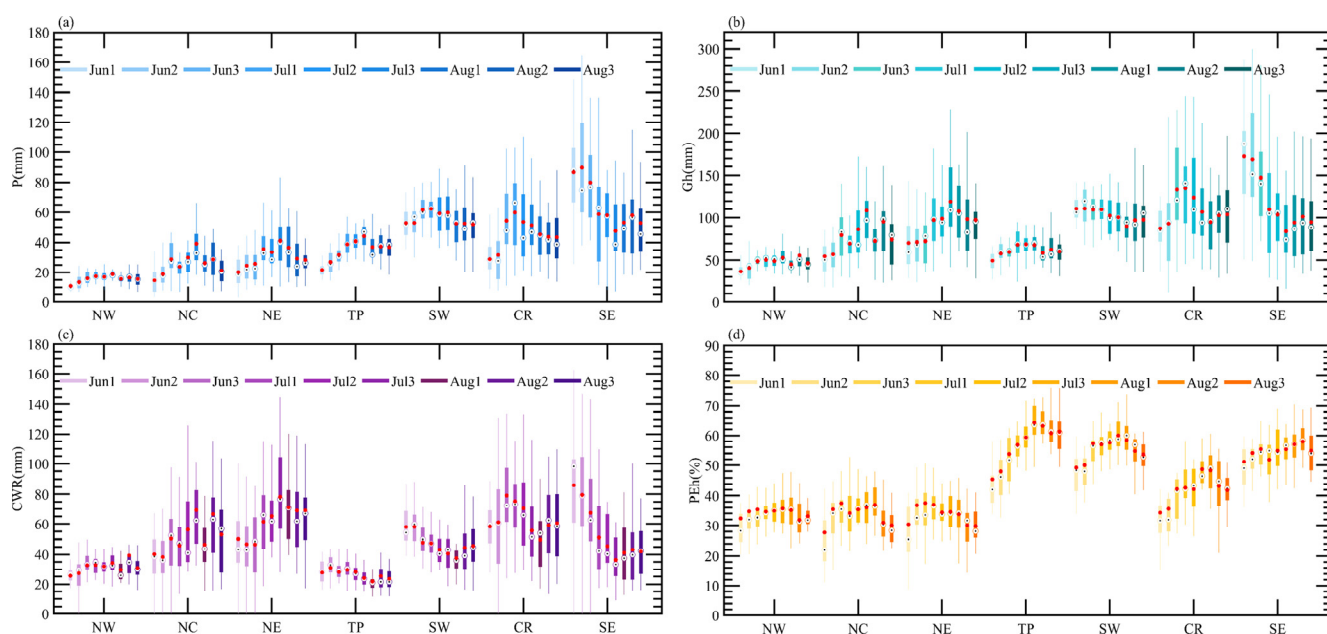


**Figure 12.** Box plot of summer ten-day variations of (a) P, (b) Gh, (c) CWR, and (d) PEh in the seven sub-regions of China during the summers of 2001–2020. The black dots in the boxes represent the median (Q3); the upper and lower sides of the boxes represent the upper quartile (Q4) and lower quartile (Q2), respectively; the upper and lower ends of the boxes' lines represent 1.5 times greater than the interquartile range ( $IQR = Q4 - Q2$ ) of the Q4 and 1.5 times less than the IQR of the Q2, representing outliers; and the red dots in the boxes represent the mean values. 1, 2, and 3 represent the early, middle, and last ten days of a month, respectively.

### 3.4. Relationship between PEh and Possible Factors in Each Sub-Region in Summer

The amount of atmospheric hydrometeors over a region and the occurrence and development of precipitation are associated with a combination of meteorological factors. Clouds are the main source of hydrometeors, so their related physical parameters have a direct impact on changes to PEh. With the continuous advancement of industrialization and urbanization, air pollution has become an increasing problem, of which aerosol pollutants are an important component. Aerosols provide the physical basis for cloud generation as water vapor condensation nuclei and facilitate the water vapor-to-cloud process, and as condensation nuclei, they facilitate the cloud-to-precipitation process and play an important role in the whole cycle of cloud development [62,63]. Thus, aerosols may also have an indirect effect on the PEh. Clarifying the correlation between PEh and some cloud physical

parameters as well as aerosols in each region is of great theoretical significance for the scientific and rational exploitation of CWR. We selected summer P and CWP, COT, Re, CTT, CTP, and AOD provided by MODIS, and the PEh of each region from 2001 to 2020 for correlation analysis and significance testing. Large correlation coefficients ( $R$ ) between PEh and some factors in a region, which passed significance tests, indicated that the PEh changes might be associated with these factors in this region. CWP indicates the abundance of CWR, COT is an important optical property parameter in clouds and is also closely related to CWC [64]. Re can reflect the distribution and variability of water droplets within clouds and has an impact on cloud microphysical processes [65], and CTT and CTP are related to the convective intensity of clouds.

The spatial distribution of  $R$  between PEh and each parameter is shown in Figure 13. PEh had a strong positive correlation with P, with  $R > 0.6$  and passing the  $\alpha = 0.05$  significance test in most regions (Figure 13a). PEh had significant (passed the 0.05 significance test) positive correlations ( $R > 0.5$ ) with CWP and COT in a few areas (Figure 13b,c). PEh was positively correlated with Re in most parts of the plateau and western NW, and south-eastern coastal areas, and it was negatively correlated with most other regions, including a significant negative correlation ( $R < -0.6$ ) in the Tianshan region (Figure 13d). In contrast, the correlation of CTT and CTP with PEh can be seen to be significantly negative in most parts of the plateau, while a strong positive correlation ( $R > 0.5$ ) was observed in western NC (Figure 13e,f). Areas with a strong positive correlation between PEh and AOD were mainly located in the NE ( $R > 0.4$ ) (Figure 13g).

Figure 14 shows the interannual variability in the relationship between PEh and each of the factors in each region. Here, the bar graphs represent the interannual variability of PEh and the line graphs with different colors represent the interannual variability of each factor. PEh and P had a moderately significant positive correlation ( $0.68 < R < 0.79$ ) in the northern regions and TP overall (Figure 14(a<sub>1</sub>,b<sub>1</sub>,c<sub>1</sub>,d<sub>1</sub>)); in SW and SE in 2007–2020 ( $R = 0.65$ ) and 2002–2020 ( $R = 0.56$ ), respectively (Figure 14(e<sub>1</sub>,g<sub>1</sub>)); and in CR in 2003–2013 ( $R = 0.64$ ) (Figure 14(f<sub>1</sub>)). In the NW, PEh had a highly significant positive correlation with CWP and CTT in 2015–2020 ( $0.83 < R < 0.87$ ) and a moderately significant positive correlation with COT in 2004–2012 ( $R = 0.76$ ) (Figure 14(a<sub>1</sub>,a<sub>2</sub>)). In the NC, PEh had a low positive correlation with AOD ( $R = 0.45$ ), a highly significant positive correlation with CWP and COT in 2014–2019 ( $0.94 < R < 0.98$ ), and a moderately significant positive correlation with CTT and CTP in 2012–2020 ( $0.65 < R < 0.69$ ) (Figure 14(b<sub>1</sub>,b<sub>2</sub>)). In the NE, PEh had a moderately significant positive correlation with CWP, COT, and AOD ( $0.44 < R < 0.53$ ) and a stronger positive correlation with Re in 2013–2020 ( $R = 0.7$ ) (Figure 14(c<sub>1</sub>,c<sub>2</sub>)). In the TP, the overall correlation between PEh and the factors was significantly weaker than in the northern regions, with a highly significant negative correlation with COT in 2015–2020 ( $R = -0.85$ ) and a moderately significant negative correlation with CTT and CTP in 2007–2020 ( $-0.7 < R < -0.67$ ) (Figure 14(d<sub>1</sub>,d<sub>2</sub>)). In CR, PEh had moderately and highly significant negative correlations with Re and AOD, respectively, in 2013–2020 ( $-0.84 < R < -0.74$ ) (Figure 14(f<sub>1</sub>,f<sub>2</sub>)).

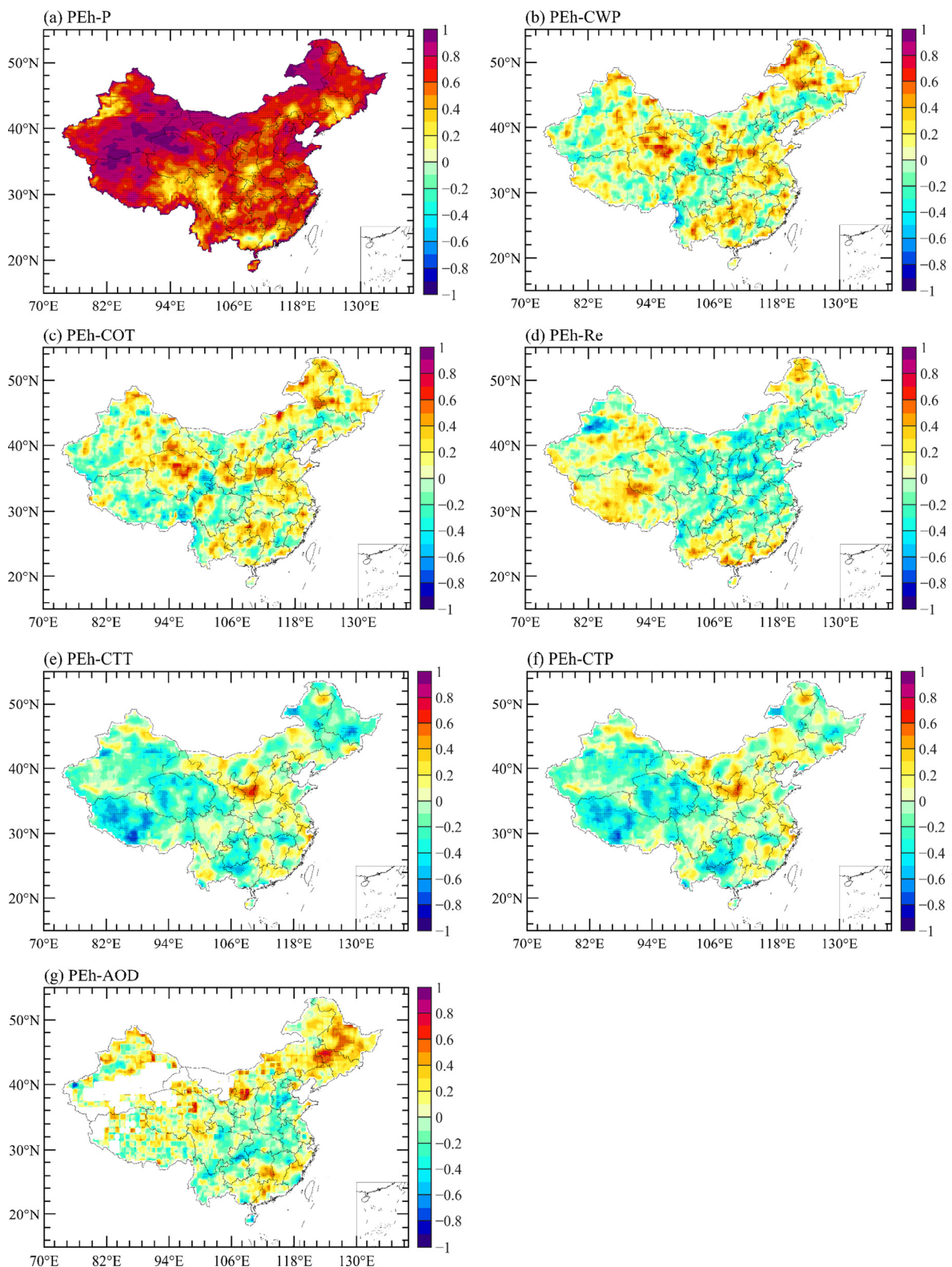


**Figure 13.** The correlation coefficient distribution between the PEh and (a) total surface precipitation (P), averaged daily (b) cloud water path (CWP), (c) cloud optical thickness (COT), (d) cloud effective radius (Re), (e) cloud top temperature (CTT), (f) cloud top pressure (CTP), and (g) aerosol optical depth over China in summer during 2001–2020. Black dots indicate the regions which passed the significance level of 0.05.



**Figure 14.** Interannual variability of the PEh (unit: %) and P (unit: mm), averaged daily CWP (unit:  $g \cdot m^{-2}$ ), COT, Re (unit:  $\mu m$ ), CTT (unit:  $^{\circ}C$ ), CTP (unit: mb), and AOD in the seven sub-regions of China in summer during 2001–2020. (a<sub>1</sub>,a<sub>2</sub>) represent NW, (b<sub>1</sub>,b<sub>2</sub>) represent NC, (c<sub>1</sub>,c<sub>2</sub>) represent NE, (d<sub>1</sub>,d<sub>2</sub>) represent TP, (e<sub>1</sub>,e<sub>2</sub>) represent SW, (f<sub>1</sub>, f<sub>2</sub>) represent CR, (g<sub>1</sub>,g<sub>2</sub>) represent SE.

The above correlation analysis shows that changes in precipitation, cloud physical parameters, and AOD in different regions can affect the spatial and temporal distribution of PEh in each region to different degrees. The correlations between PEh and each factor for each region in the last 20 years are summarized in Figure 15.

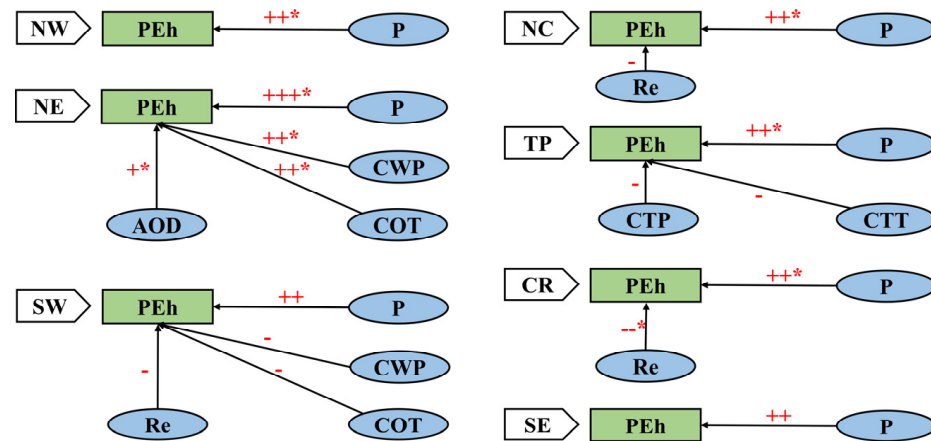


**Figure 15.** A schematic representation of the possible factors which influence summer PEh in the seven sub-regions of China. The red +\*, -, ++, +++, --\*, +++\* represent low increase passed 0.05 significance level, low decrease, moderate increase, moderate increase passed 0.05 significance level, moderate decrease passed 0.05 significance level, high increase passed 0.05 significance level, respectively.

#### 4. Conclusions and Discussion

In this study, using ground precipitation, high spatial and temporal resolution ERA5 reanalysis, and MODIS satellite remote sensing data and having divided China into seven regions, we first examined the long-term trends of PW, cloud cover, and total column CWC in each region from 1979 to 2020. Then, we analyzed variations at different time scales of CWR characteristic quantities in summer over the past 20 years. Finally, we explored the possible factors affecting PEh in each region. The following preliminary conclusions were obtained.

(1) In the last 42 summers, the areas with significant increases of PW were located in the plateau and surrounding areas and were distributed along mountain ranges, including NW and TP. Both cloud cover and total column CWC decreased significantly in NC and increased significantly in TP (except for medium-cloud cover);

(2) In the past 20 summers, PEh in most regions of China (except NW and TP) increased significantly and had obvious interdecadal variation. In 2001, PEh was low in all regions. In NW, PEh was predominantly high after 2002. In NC, NE, and SE, PEh was predominantly low in the first 10 years, but after 2011, PEh increased, and positive anomalies occurred more often. In TP, PEh was predominantly high in the first 10 years, and the difference between positive and negative anomalies was lower in the second decade. In SW and CR, there were more, larger negative anomalies before 2004, and anomalies were high in most years thereafter. CWR decreased relatively faster in NC, SW, CR, and SE, and increased in NE and TP. The monthly variations showed that, in June, TP, SW, CR, and SE had low PEh and more CWR, and their CWR exploitation potential was higher. CWR exploitation potential was also higher in August in the northern regions. Analysis of ten-day variation revealed that in TP, SW, and CR, PEh peaks and CWR troughs occurred in late July or early August, while in SE, PEh varied within a smaller range and increased overall. CWR showed a decreasing trend in June and July and an insignificant change in August;

(3) The correlation between PEh and each factor has clear regional features. PEh was largely influenced by P in each region ( $0.55 < R < 0.82^*$ ). In NE, it had a moderate and low significant positive correlation with CWP, COT, and AOD ( $0.44^* < R < 0.54^*$ ), and in CR it had a moderate significant negative correlation with Re ( $R = -0.54^*$ ).



This study focused on the spatial and temporal characteristics of AWR in China during summer, which could be combined with other seasons for comparative analysis in future studies, in order to systematically analyze the exploitation potential and conditions of CWR. For the study of the multi-temporal scale variation characteristics of CWR, diurnal variation was not considered. Future studies can shorten the temporal scale to hours to analyze the occurrence of any significant daily variation in CWR and PEh. To explore the possible factors influencing PEh, a short time frame and a single statistical method were selected. Future studies could use data from a long time series and multiple analysis methods for more in-depth analysis, which would be important to guide local meticulous weather modification activities.

**Author Contributions:** Conceptualization, Z.Y. and L.A.; methodology, L.A. and Z.Y.; software, L.A.; validation, L.A. and Z.Y.; formal analysis, L.A. and P.Z.; investigation, P.Z. and S.J.; resources, Z.Y.; data curation, S.J., J.Z., Z.L. and Z.Z.; writing—original draft preparation, L.A.; writing—review and editing, Z.Y.; visualization, S.J., J.Z., Z.L. and Z.Z.; supervision, Z.Y.; project administration, Z.Y.; funding acquisition, Z.Y. All authors have read and agreed to the published version of the manuscript.

**Funding:** This research was funded by the National Natural Science Foundation of China (No: 41775139) and Ministry of Science and Technology of China (Nos: 2016YFE0201900 and GYHY201406033).

**Data Availability Statement:** Publicly available datasets were analyzed in this study. These data can be found here in the DEM of China from Resource and Environment Science and Data Center, at <http://www.resdc.cn/> (accessed on 28 January 2021). The grid-based precipitation data presented in this study are openly available in the National Meteorological Information Center of China, at <http://data.cma.cn/> (accessed on 28 January 2021). The reanalysis data were provided by the Copernicus Climate Data Store, at <http://cds.climate.copernicus.eu/> (accessed on 28 January 2021). Satellite data provided by the Level-1 and Atmosphere Archive and Distribution System Distributed Active Archive Center, at <https://ladsweb.modaps.eosdis.nasa.gov/search/> (accessed on 28 January 2021).

**Acknowledgments:** The authors sincerely appreciate anonymous reviewers for their valuable comments and suggestions that helped improve the quality of our manuscript.

**Conflicts of Interest:** The authors declare no conflict of interest.

## References

1. Li, X.; Guo, X.; Zhu, J. Climatic Distribution Features and Trends of Cloud Water Resources over China. *Chin. J. Atmos. Sci.* **2008**, *32*, 1094–1106. (In Chinese)
2. An, L.; Yao, Z.; Zhang, P.; Jia, S.; Zhao, J.; Gao, L.; Liu, Z. Regional characteristics and exploitation potential of atmospheric water resources in China. *Int. J. Climatol.* **2022**, *42*, 3225–3245. [[CrossRef](#)]
3. Chahine, M.T. The hydrological cycle and its influence on climate. *Nature* **1992**, *359*, 373–380. [[CrossRef](#)]
4. Cao, L.; Yu, J.; Ge, Z. Water vapor content in the atmosphere and its variation trend over North China. *Adv. Water Sci.* **2005**, *16*, 439–443. (In Chinese)
5. Li, J.; Xu, Q.; Zhan, J.; Wei, H. Atmospheric precipitable water vapor at several typical zones in China. *Infrared. Laser Eng.* **2012**, *41*, 3055–3060. (In Chinese)
6. Ma, X.; Shang, K.; Li, J.; Wang, J.; Kang, Y.; Wang, S. Spatial and Temporal Changes of Atmospheric Precipitable Water in the Eastern Part of Northwest China from 1981 to 2010. *J. Desert Res.* **2015**, *35*, 448–455. (In Chinese)
7. Huang, X.; Wang, S.; Wang, X. Variations of Precipitable Water in Northwest China During 1960–2015. *Meteor. Mon.* **2018**, *44*, 1191–1199. (In Chinese)
8. Zhu, B.; Zhang, Q.; Lu, G.; Li, D.; Li, C. Analysis of the distribution characteristics and trend of air vapor in Qilian Mountains. *Plateau Meteor.* **2019**, *38*, 935–943. (In Chinese)
9. Zhou, C.; Jiang, X.; Li, Y.; Wei, G. Features of Climate Change of Water Vapor Resource over Eastern Region of the Tibetan Plateau and Its Surroundings. *Plateau Meteor.* **2009**, *28*, 55–63. (In Chinese)
10. Zhou, S.; Wu, P.; Wang, C.; Han, J. Spatial distribution of atmospheric water vapor and its relationship with precipitation in summer over the Tibetan Plateau. *J. Geogr. Sci.* **2012**, *22*, 795–809. [[CrossRef](#)]
11. Chang, S.; Liu, Y.; Hua, S.; Jia, R. Characteristics of atmospheric water vapor over the Qinghai-Tibetan Plateau in summer with global warming. *Plateau Meteor.* **2019**, *38*, 227–236. (In Chinese)
12. Kaiser, D.P. Decreasing cloudiness over China: An updated analysis examining additional variables. *Geophys. Res. Lett.* **2000**, *27*, 2193–2196. [[CrossRef](#)]
13. Wang, H.; Chen, Y.; Peng, K.; Cui, C.; Zhang, G.; Liu, Q. Study on Cloud Water Resources of Mountain Ranges in Xinjiang Based on Aqua Satellite Data. *J. Nat. Resour.* **2011**, *26*, 89–96. (In Chinese)

14. Zhang, Q.; Li, Y.; Chen, Q.; Ren, J. Temporal and Spatial Distributions of Cloud Cover over Southwest China in Recent 46 Years. *Plateau Meteor.* **2011**, *30*, 339–348. (In Chinese)
15. Li, J.; Jian, B.; Zhao, C.; Zhao, Y.; Wang, J.; Huang, J. Atmospheric instability dominates the long-term variation of cloud vertical overlap over the Southern Great Plains site. *J. Geophys. Res.-Atmos.* **2019**, *124*, 9691–9701. [[CrossRef](#)]
16. Mao, K.B.; Yuan, Z.J.; Zuo, Z.Y.; Xu, T.R.; Shen, X.Y.; Gao, C.Y. Changes in global cloud cover based on remote sensing data from 2003 to 2012. *Chin. Geogr. Sci.* **2019**, *29*, 306–315. [[CrossRef](#)]
17. Lee, S.; Kim, S.W.; Hwang, S.O.; Choi, J.N.; Ahn, K.B.; Kim, J. Comparative Analysis of the Cloud Behavior over Inland and Coastal Regions within Single Climate Characteristics. *Atmosphere* **2020**, *11*, 1316. [[CrossRef](#)]
18. Liu, Y.; Wang, N.; Wu, X.; Guo, Z.; He, J. Temporal and Spatial Characteristics and Influence Factors of Low Cloud Amount over China in 1951–2009. *Plateau Meteor.* **2013**, *32*, 1608–1616. (In Chinese)
19. Liu, B.; Li, D. Spatio-Temporal Variation Features of Cloud Cover in China and Its Correlation to North Boundary Belt of Subtropical Summer Monsoon. *Meteor. Mon.* **2018**, *44*, 382–395. (In Chinese)
20. Fu, C.; Dan, L.; Feng, J.; Peng, J.; Ying, N. Temporal and spatial variations of total cloud amount and their possible relationships with temperature and water vapor over China during 1960 to 2012. *Chin. J. Atmos. Sci.* **2019**, *43*, 87–98. (In Chinese)
21. Su, Y.; Zhao, C.; Wang, Y.; Ma, Z. Spatiotemporal variations of precipitation in China using surface gauge observations from 1961 to 2016. *Atmosphere* **2020**, *11*, 303. [[CrossRef](#)]
22. Wu, C.; Liu, L.; Chen, C.; Zhang, C.; He, G.; Li, J. Challenges of the polarimetric update on operational radars in China—Ground clutter contamination of weather radar observations. *Remote Sens.* **2021**, *13*, 217. [[CrossRef](#)]
23. Li, Y.; Yu, R.; Xu, Y.; Zhang, X. Spatial distribution and seasonal variation of cloud over China based on ISCCP data and surface observations. *J. Meteor. Soc. Japan* **2004**, *82*, 761–773. [[CrossRef](#)]
24. Li, J.M.; Jian, B.D.; Huang, J.P.; Hu, Y.X.; Zhao, C.F.; Kawamoto, K.; Liao, S.J.; Wu, M. Long-term variation of cloud droplet number concentrations from space-based Lidar. *Remote Sens. Environ.* **2018**, *213*, 144–161. [[CrossRef](#)]
25. Zhao, C.F.; Chen, Y.Y.; Li, J.M.; Letu, H.S.; Su, Y.F.; Chen, T.M.; Wu, X.L. Fifteen-year statistical analysis of cloud characteristics over China using Terra and Aqua Moderate Resolution Imaging Spectroradiometer observations. *In. J. Climatol.* **2019**, *39*, 1–18. [[CrossRef](#)]
26. Ma, Q.; You, Q.; Ma, Y.; Cao, Y.; Zhang, J.; Niu, M.; Zhang, Y. Changes in cloud amount over the Tibetan Plateau and impacts of large-scale circulation. *Atmos. Res.* **2021**, *249*, 105332. [[CrossRef](#)]
27. Yang, Y.; Zhao, C.; Fan, H. Spatiotemporal distributions of cloud properties over China based on Himawari-8 advanced Himawari imager data. *Atmos. Res.* **2020**, *240*, 104927. [[CrossRef](#)]
28. Zhou, X.; Zhang, H.; Jing, X. Distribution Variation Trends of Cloud Amount and Optical Thickness over China. *J. Atmos. Environ. Optics* **2016**, *11*, 1–13. (In Chinese)
29. Fan, S.; Wang, W.; Lin, D. Temporal and Spatial Distribution Characteristics of Clouds with Different Types over China Based on ISCCP Data. *J. Arid Meteor.* **2020**, *38*, 213–225. (In Chinese)
30. You, T.; Zhang, H.; Wang, H.; Zhao, M. Distribution of Different Cloud Types and Their Effects on Near-Surface Air Temperature during Summer Daytime in Central Eastern China. *Chinese J. Atmos. Sci.* **2020**, *44*, 835–850. (In Chinese)
31. Liu, J.; You, Q.; Zhou, Y.; Ma, Q.; Cai, M. Distribution and trend of cloud water content in China based on ERA-Interim reanalysis. *Plateau Meteor.* **2018**, *37*, 1590–1604. (In Chinese)
32. Liu, J.; You, Q.; Wang, N. Interannual anomaly of cloud water content and its connection with water vapor transport over the Qinghai-Tibetan Plateau in summer. *Plateau Meteor.* **2019**, *38*, 449–459. (In Chinese)
33. He, X.; Song, M.; Zhou, Z. Temporal and Spatial Characteristics of Water Vapor and Cloud Water over the Qinghai Tibetan Plateau in Summer. *Plateau Meteor.* **2020**, *39*, 1339–1347. (In Chinese)
34. You, Q.; Liu, J.; Nike, P. Changes of summer cloud water content in China from ERA-Interim reanalysis. *Glob. Planet. Change* **2019**, *175*, 210. [[CrossRef](#)]
35. Cheng, J.; You, Q.; Cai, M.; Sun, J.; Zhou, Y. Cloud Water Resource over the Asian water tower in recent decades. *Atmos. Res.* **2022**, *269*, 106038. [[CrossRef](#)]
36. Sui, C.-H.; Satoh, M.; Suzuki, K. Precipitation Efficiency and its Role in Cloud-Radiative Feedbacks to Climate Variability. *J. Meteor. Soc. Japan Ser. II* **2020**, *98*, 261. [[CrossRef](#)]
37. Wang, J.; Gui, S.; Ma, A.; Yang, R.; Zhang, Q. Interdecadal variability of summer precipitation efficiency in east Asia. *Adv. Meteor.* **2019**, *2019*, 3563024. [[CrossRef](#)]
38. Wu, Y.C.; Yang, M.J.; Lin, P.H. Evolution of water budget and precipitation efficiency of mesoscale convective systems over the South China Sea. *Terr. Atmos. Ocean. Sci.* **2020**, *31*, 141–158. [[CrossRef](#)]
39. Zhou, Y.; Cai, M.; Tan, C.; Mao, J.; Hu, Z. Quantifying the Cloud Water Resource: Basic Concepts and Characteristics. *J. Meteor. Res.* **2020**, *34*, 1242–1255. [[CrossRef](#)]
40. Zhang, Y.; Li, B.; Chen, Y. The Temporal and Spatial Variation of Water Vapor Content and Its Relationship with Precipitation in the Arid Region of Northwest China from 1970 to 2013. *J. Nat. Res.* **2018**, *33*, 1043–1055. (In Chinese)
41. Cai, M.; Zhou, Y.; Liu, J.; Tang, Y.; Tan, C.; Zhao, J.; Ou, J. Diagnostic quantification of the cloud water resource in China during 2000–2019. *J. Meteor. Res.* **2022**, *36*, 292–310. [[CrossRef](#)]
42. Zhao, Y.; Zhu, J. Assessing quality of grid daily precipitation datasets in China in recent 50 year. *Plateau Meteor.* **2015**, *34*, 50–58. (In Chinese)

43. Zhang, P.; Yao, Z.; Jia, S.; Chang, Z.; Sang, J.; Gao, L.; Zhao, W.; Wang, W.; Zhu, X. Study of the characteristics of atmospheric water resources and hydrometeor precipitation efficiency over the Liupan Shan area. *Chin. J. Atmos. Sci.* **2020**, *44*, 421–434. (In Chinese)
44. Hersbach, H.; Bell, B.; Berrisford, P.; Biavati, G.; Horányi, A.; Muñoz-Sabater, J.; Nicolas, J.; Peubey, C.; Radu, R.; Rozum, I.; et al. *ERA5 Monthly Averaged Data on Single Levels from 1979 to Present*; Copernicus Climate Change Service (C3S) Climate Data Store (CDS): Reading, UK, 2019. [[CrossRef](#)]
45. Hersbach, H.; Bell, B.; Berrisford, P.; Biavati, G.; Horányi, A.; Muñoz-Sabater, J.; Nicolas, J.; Peubey, C.; Radu, R.; Rozum, I.; et al. *ERA5 Hourly Data on Pressure Levels from 1979 to Present*; Copernicus Climate Change Service (C3S) Climate Data Store (CDS): Reading, UK, 2018. [[CrossRef](#)]
46. Hersbach, H.; Bell, B.; Berrisford, P.; Hirahara, S.; Horányi, A.; Muñoz-Sabater, J.; Nicolas, J.; Peubey, C.; Radu, R.; Schepers, D.; et al. The ERA-5 global reanalysis. *QJR Meteorol. Soc.* **2020**, *146*, 1999–2049. [[CrossRef](#)]
47. Sun, Y.; Zhao, C. Influence of Saharan dust on the large-scale meteorological environment for development of tropical cyclone over North Atlantic Ocean Basin. *J. Geophys. Res. Atmos.* **2020**, *125*, e2020JD033454. [[CrossRef](#)]
48. Shen, L.; Zhao, C.; Yang, X. Insight into the seasonal variations of the sea-land breeze in Los Angeles with respect to the effects of solar radiation and climate type. *J. Geophys. Res. Atmos.* **2021**, *126*, e2020JD033197. [[CrossRef](#)]
49. Xia, Y.; Wang, Y.; Huang, Y.; Hu, Y.; Bian, J.; Zhao, C.; Sun, C. Significant contribution of stratospheric water vapor to the poleward expansion of the Hadley circulation in autumn under greenhouse warming. *Geophys. Res. Lett.* **2021**, *48*, e2021GL094008. [[CrossRef](#)]
50. Platnick, S.; King, M.; Hubanks, P. *MODIS Atmosphere L3 Daily Product*; NASA MODIS Adaptive Processing System; Goddard Space Flight Center: Greenbelt, MA, USA, 2017.
51. Meyer, K.; Yang, P.; Gao, B.C. Tropical ice cloud optical depth, ice water path, and frequency fields inferred from the MODIS level-3 data. *Atmos. Res.* **2007**, *85*, 171–182. [[CrossRef](#)]
52. Bao, S.; Letu, H.; Zhao, C.; Tana, G.; Shang, H.; Wang, T.; Lige, B.; Bao, Y.; Purevjav, G.; He, J.; et al. Spatiotemporal distributions of cloud parameters and the temperature response over the Mongolian Plateau during 2006–2015 based on MODIS data. *IEEE J. Sel. Top. Appl. Earth Observ. Remote Sens.* **2018**, *12*, 549–558. [[CrossRef](#)]
53. Bao, S.; Letu, H.; Zhao, J.; Sheng, H.; Lei, Y.; Duan, A.; Chen, B.; Bao, Y.; He, J.; Wang, T.; et al. Spatiotemporal distributions of cloud parameters and their response to meteorological factors over the Tibetan Plateau during 2003–2015 based on MODIS data. *Int. J. Climatol.* **2019**, *39*, 532–543. [[CrossRef](#)]
54. Mudelsee, M. *Climate Time Series Analysis: Classical Statistical and Bootstrap Methods*, 2nd ed.; Springer: Dordrecht, Netherlands; Heidelberg, Germany; London, UK; New York, NY, USA, 2014; ISBN 978-3-319-04449-1.
55. Mann, H.B. Non-Parametric Test against Trend. *Econometrica* **1945**, *13*, 245–259. [[CrossRef](#)]
56. Kendall, M.G. *Rank Correlation Methods*, 4th ed.; Charles Griffin: London, UK, 1975.
57. Sen, P.K. Estimates of the Regression Coefficient Based on Kendall’s Tau. *J. Am. Stat. Assoc.* **1968**, *63*, 1379–1389. [[CrossRef](#)]
58. Wang, S.; Xu, T.; Nie, W.; Jiang, C.; Yang, Y.; Fang, Z.; Li, M.; Zhang, Z. Evaluation of Precipitable Water Vapor from Five Reanalysis Products with Ground-Based GNSS Observations. *Remote Sens.* **2020**, *12*, 1817. [[CrossRef](#)]
59. Zhang, D.; Shi, C.; Zhang, T.; Shen, R.; Wang, Z. Comparative Analysis of the Total Cloud Cover Products of Various Data in China. *Plateau Meteor.* **2022**, *41*, 803–813. (In Chinese)
60. Taylor, K.E.; Ghan, S.J. An analysis of cloud liquid water feedback and global climate sensitivity in a general circulation model. *J. Clim.* **1992**, *5*, 907–919. [[CrossRef](#)]
61. Shupe, M.D.; Intrieri, J.M. Cloud radiative forcing of the Arctic surface: The influence of cloud properties, surface albedo, and solar zenith angle. *J. Clim.* **2004**, *17*, 616–628. [[CrossRef](#)]
62. Albrecht, B.A. Aerosols, cloud microphysics, and fractional cloudiness. *Science* **1989**, *245*, 1227–1230. [[CrossRef](#)]
63. Han, Q.; Rossow, W.B.; Zeng, J.; Welch, R. Three different behaviors of liquid water path of water clouds in aerosol-cloud interactions. *J. Atmos. Sci.* **2002**, *59*, 726–735. [[CrossRef](#)]
64. Roeckner, E.; Schlese, U.; Biercamp, J.; Loewe, P. Cloud optical depth feedbacks and climate modelling. *Nature* **1987**, *32*, 138–140. [[CrossRef](#)]
65. Yang, B.; Zhang, H.; Peng, J.; Wang, Z.; Jin, X. Analysis on Global Distribution Characteristics of Cloud Microphysical and Optical Properties Based on the CloudSat Data. *Plateau Meteor.* **2014**, *33*, 1105–1118. (In Chinese)

**Disclaimer/Publisher’s Note:** The statements, opinions and data contained in all publications are solely those of the individual author(s) and contributor(s) and not of MDPI and/or the editor(s). MDPI and/or the editor(s) disclaim responsibility for any injury to people or property resulting from any ideas, methods, instructions or products referred to in the content.